ITO and AZO films for low emissivity coatings in hybrid photovoltaic-thermal applications

DIEGO ALONSO-ÁLVAREZ,[1,*] LOURDES FERRE LLIN,[2] ALEXANDER MELLOR,[1] DOUGLAS J. PAUL,[2] AND NICHOLAS J. EKINS-DAUKES[1]

[1]*Imperial College London, Department of Physics, London SW7 2AZ, United Kingdom*
[2]*University of Glasgow, School of Engineering, Glasgow G12 8LT, United Kingdom*
**d.alonso-alvarez@imperial.ac.uk*

Abstract: We report on the electrical and optical properties of ITO and AZO films fabricated directly on silicon substrates under several growth and annealing temperatures. We use broadband spectroscopic ellipsometry measurements (from 300 nm to 20 μm) to obtain a consistent model for the permittivity of each of the films. The results are then used to design an optimized, single layer, high transparency, high conductivity film, suitable as front transparent electrode and low thermal emissivity coating for silicon based solar cells. The best performance is found using the properties of the ITO film grown at 250 ºC, with a state of the art resistivity of 0.2 mΩ-cm and an optimized thickness of 75 nm which leads to 0.79 average absorptivity in the solar range (300-2000 nm) and 0.21 average emissivity in the thermal range (5-20 μm). The structural characterization of the films using X-Ray diffraction, and the Hall mobility and resistivity measurements of all the films are also provided, complementing and supporting the observed optical properties.

Keywords: silicon, transparent conductive oxide, photovoltaics, solar thermal

1. Introduction

Transparent conductive oxides (TCO) are at the heart of modern optoelectronic devices [1]. They are an essential component of displays and touchscreens in tablets and mobile phones. They are also key materials in light-emitting diodes as well as in photovoltaics; they form the front electrode in many solar cell technologies: either inorganic thin film solar cells (CIGS, CdTe, amorphous silicon) [2], organic [3] or even the state of the art silicon heterojunction devices [4]. For most of these applications, the specifications of the TCO layers are quite rigid: they must have very high transparency over a broad spectral range, and possess excellent electrical transport properties. Long term stability and low cost, especially for large area applications such as photovoltaics (PV), is also an essential.

TCOs also have applications related to their wavelength-selective reflectivity. TCOs are widely used in architecture for energy efficient windows, either as static films to control thermal emissivity [5] or in smart windows [6], to control the solar gain. The use of TCOs in solar energy extends also to solar thermal collectors, where the purpose is to allow all sunlight to enter in the collector and prevent radiative heat loss. For example, Ehrmann et al. [7] optimized aluminium-doped ZnO (AZO) films for a double-glazed flat-plate collector, achieving solar transmittance of 0.85 while keeping an infrared emissivity as low as 0.3. A more recent application is their use in hybrid PV-Thermal (PVT) solar systems where they restrict radiative heat loss without compromising PV performance [8-12]. The design of suitable spectrally selective coatings for this application has been recently tackled by Lämmle et al. [8], using a multilayered coating combining both AZO and silver layers to achieve high transparency (>0.8) in the solar spectrum while keeping as low as 0.13 emissivity in the mid-infrared (MIR) region.

In Lämmle's work – and references therein – the low emissivity coating is applied to the glass of the PVT laminate as part of a double-glazed PVT collector [8]. There are, however, situations where applying the coating directly to the solar cells is more convenient. This is the case for hybrid PVT systems based on evacuated tubes, either using the global solar spectrum

or under concentration for higher operating temperatures [10]. In this case, encapsulants on the front side of the cell (typically ethylene-vinyl acetate (EVA) and glass) are absent, convective losses are almost completely suppressed and the only heat loss comes from thermal radiative emission from the surface of the solar cell [11]. Silicon heterojunction technologies (SHJ) moreover already use TCO as a front electrode and anti-reflective (AR) coating [13,14], and generally demonstrate a lower thermal coefficient than normal crystalline or polycrystalline silicon solar cells. These two properties suggest SHJ as the best choice for hybrid systems aiming to work at 80-120 ºC since they incorporate the TCO as a key element, and there is only a need to optimize the TCO properties for the additional functionality of low emissivity coating.

In this work, we study the two most common TCOs, indium tin oxide (ITO) and aluminium zinc oxide (AZO), in the context of hybrid PVT systems. The goal is to determine the performance of the materials as both, a front transparent electrode for absorbing the solar spectrum and working as current transport layer, and as a low emissivity coating for blackbody thermal radiation.

ITO is the TCO of choice in many optoelectronic applications, but its high cost due in part to the scarcity of indium and its poor stability under certain processing conditions motivates the study of other materials. As a consequence, AZO and other alloys such as Ga-doped ZnO [15,16] or Sb-doped SnO2 [17], are beginning to displace ITO, especially for applications that require large surface area at low costs. So far, the intense research in this field has focused on studying the electrical performance and the transparency in the visible and near infrared (300-2000 nm), as the two most relevant properties for visual displays and solar energy applications. Existing literature covers the impact of the fabrication method and deposition conditions[7,14,18-23], the post-processing of the film (such as high temperature annealing treatments) [15,17,24-28] or the role of the substrate in governing the properties of the TCOs [29,30]. In respect to the latter, most works use glass or SiO_2 as substrates [19,23,24,31-34] or, more recently, flexible, lightweight materials like PET or PEN [30]. However, it is shown in these reports that the substrate plays a key role in the properties of the film and therefore it cannot be concluded that those films will have the same properties when grown on the actual substrate of interest. In the case of solar cells, that substrate could be silicon, as in SHJ solar cells, or other polycrystalline semiconductors, such as CIGS or CdTe.

The present work analyses the optical properties of ITO and AZO films grown directly on silicon substrates using, to that purpose, spectroscopic ellipsometry. Contrary to the usual transmission measurements performed on transparent substrates, this technique is purely reflective and provides more fundamental information about the properties of the films – the dielectric function of the materials – which can be used later for modelling, simulation and subsequent optimization of photovoltaic devices. Moreover, our work covers not only the solar spectral range (300-2000 nm) but also the mid-infrared range (6-12 μm), region of interest in solar thermal applications, and correlates that with the electrical properties of the films, key for excellent current transport.

2. Experimental details

The films were grown on an Angstrom RF magnetron sputtering system. The base pressure was $<5x10^{-6}$ mbar and the process pressure under argon atmosphere was of 2.6 mbar. The distance between the target (7.62 cm in diameter) and the rotating sample holder was about 15 cm. The ITO target had a 99.99% purity and was made of a mixture of indium oxide and tin oxide (In_2O_3/SnO_2 90/10 WT%, Kurt J. Lesker). The AZO target also had a 99.99% purity and was made of zinc oxide and aluminium oxide (ZnO/Al_2O_3 98/2 WT%, Testbourne Ltd). The growth rates for the ITO and AZO films were 0.7 Å/s and 0.8 Å/s, corresponding to sputter powers of 118 W and 300 W, respectively. The substrates were high resistivity p-type silicon (100), 100 cm in diameter and 450 μm thick. For the films grown at room temperature, a full wafer was used for each of the two materials and then diced into smaller pieces to perform the different

annealing processes. Together with the silicon wafers, a calibration sample was used in each case to measure the thickness of the films. Further samples of the two materials were grown at 150ºC, 250ºC and 350ºC respectively. In this case, the substrate was diced prior to the film deposition. The rapid thermal processing was carried out in a SSI Inc Solaris 150 Rapid Thermal Processing System under N_2 atmosphere. Five annealing temperatures were used: 400 ºC, 500 ºC, 600 ºC, 700 ºC and 800 ºC, and the annealing time was 3 min in all cases. These annealing temperatures were chosen as they cover the usual range often found in the literature for these materials. However, there is indeed a large variation in the annealing times – from 30 s to 2 hours –, atmospheres – N_2, O_2, forming gas, air – and the effect that such high temperature processing have in the films [15,17,24-28].

X-Ray diffraction (XRD) measurements were performed on a Panalytical X'Pert Pro MRD system with a rotating stage. The grain size in the out of plane direction is calculated using the Scherrer's formula with a reference peak width of 0.12º [26]. Scanning electron microscope (SEM) images were taken with a LEO Gemini 1525 FEGSEM system. Ellipsometry analysis was performed using two J. A. Woollam Co. systems, a V-VASE for the UV-VIS-NIR range (300 nm - 1700 nm) and a IR-VASE Mark-II for the MIR (1.7 µm – 20 µm). Ellipsometric parameters were taken at three angles (45º, 60º and 75º). The data from the two systems was combined and fitted to the modelled dielectric function over the whole spectral range (300 nm to 20 µm wavelength) using the WVASE software from J.A. Woollam Co.. For these experiments, the back of the samples was mechanically roughened to reduce reflections from the back surface. Despite the roughening, in some cases there was some depolarization for the longest wavelengths and the 75º measurements. Those data points were excluded from the fitting process. The sample size was around 20x20 mm^2 and a minimum spot size for the infrared measurements was 8 mm.

Two setups were employed for the electrical characterization of the films: the resistivity ρ was measured using a 4-point probe Jandel RM2 system in a linear configuration with a probe separation of 1 mm; resistivity and mobility, μ, were also characterized using a Nanometrics HL5500 Hall system in the Van der Pauw configuration. The carrier density, N, was calculated from the Hall results as $N = (q\mu\rho)^{-1}$, where q is defined as the electron charge. For these measurements, the samples were cleaved into square pieces of 5x5 mm^2.

3. Results

3.1 Structural Properties: X-ray diffraction and SEM

Fig. 1 shows the XRD patterns for the ITO samples. Films grown at room temperature are amorphous yet develop a crystalline structure as soon as they are annealed or grown at higher temperatures. The 150 ºC film (Fig. 1a) shows crystals with preferential (400) plane orientation, while the 350 ºC grows with the (211) orientation. The pattern for the 250 ºC sample demonstrated the highest randomization for the orientation of the grains, although with some preference for the (400) compared with a powder reference. These observations agree with the variety of behaviours observed in the literature for different growth conditions and substrates [24,25,34]. The position and width of the peaks indicate that the films are relaxed and have grain size on the order of 28 nm in all cases. Part of the material is still in the amorphous phase given the low intensity of the peaks relative to the substrate and high background of the XRD patterns. On the other hand, the annealed films (Fig. 1b) all demonstrate excellent crystalline structure formed of randomly oriented grains and with very low background associated to the amorphous phases. The intensity ratio of the peaks and their angular position are compatible with those of cubic In_2O_3 (ICSD collection code 033649). The peaks are all slightly shifted to higher angles, though, characteristic of films under tensile stress. A detail of the (222) diffraction peak is shown in Fig. 1c, where it is clear that the shift is essentially constant for all annealing temperatures. Given the similar size of In and Sn atoms, the shift is likely to be related

to oxygen vacancies in the crystal lattice. The width of the peak is homogeneous and very narrow, indicating that the grains extend the whole thickness of the film (~100 nm).

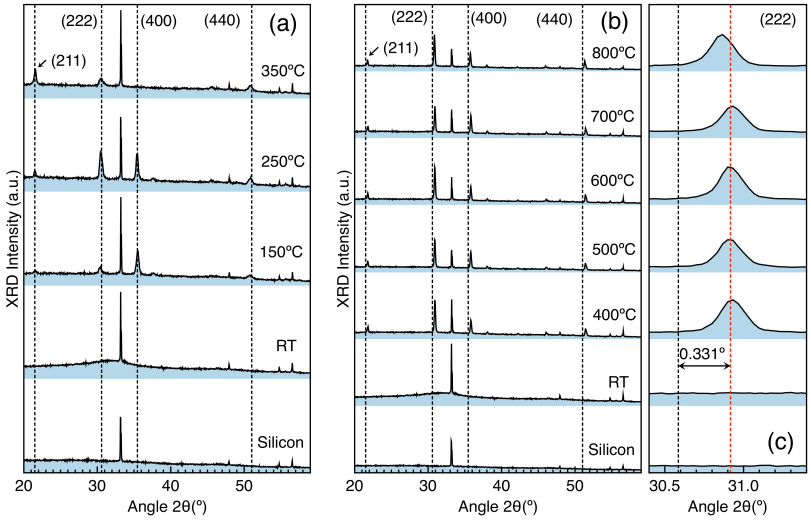

Fig. 1. XRD patterns of the ITO films: (a) grown at different temperatures and (b) grown at RT and annealed. (c) Detail of the shift of the (222) diffraction peak of the annealed samples. The vertical dashed lines indicate the position of the diffraction peaks in a powder sample.

Contrary to ITO, AZO films (Fig. 2) always grow as an hexagonal, crystalline phase, with preferential (002) orientation, as it is often observed under different growth conditions and substrates [21,35]. There are no peaks associated with other chemical species in any of the films (eg. Al_2O_3 or metallic Al). As the growth temperature increases (Fig. 2a), the peaks shift to a higher angle compared with the peak positions of the ZnO reference (ICSD collection code 026170). More importantly, the intensity increases by up to one order of magnitude in the case of the 350 ºC sample compared to the room temperature grown sample. These points show an extraordinary increase in crystallinity and orientation of the grains with substrate temperature. The width of the peaks related to the vertical grain size, however, does not change significantly, resulting always in values in the 30-40 nm range. With increasing annealing temperature (Fig. 2b), the peak also shifts towards higher angles and narrows. This trend is associated with the substitution of Zn atoms in the crystal lattice by Al atoms, which are smaller and lead to tensile strain, and also to the appearance of oxygen vacancies. Both processes also result in higher carrier density and lower resistivity in the film, as it will be shown below. Thermal stress might also play a role given the large differences between the thermal expansion coefficient of silicon and AZO (2.6×10^{-6} K^{-1} and $\sim9.0\times10^{-6}$ K^{-1}, respectively [29,30]). The intensity of the peaks of all annealed samples is around the same order of magnitude, contrary to the high temperature grown samples.

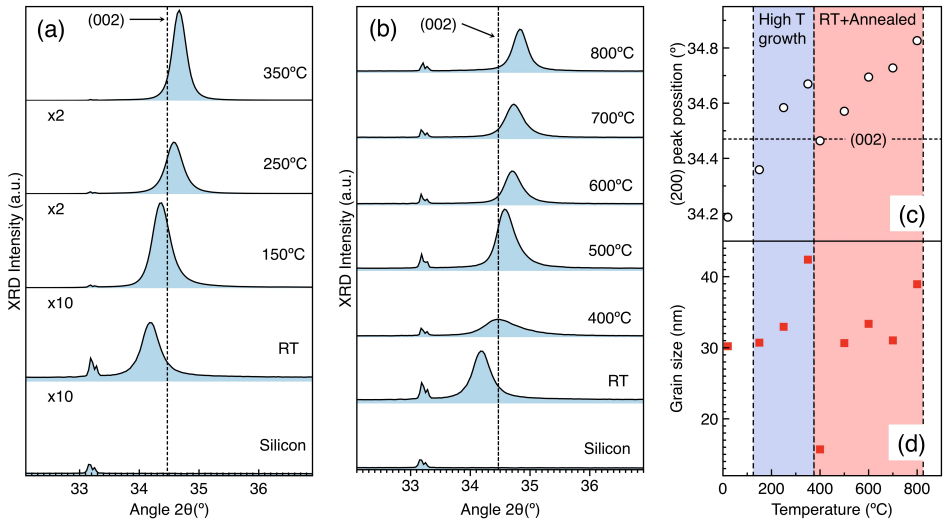

Fig. 2. XRD patterns of the AZO films: (a) grown at different temperatures, (b) grown at RT and annealed, (c) position of the (002) diffraction peak and (d) the calculated grain size.

Figure 3 shows two selected SEM images corresponding to the ITO and AZO films grown at 250 ºC and 350 ºC, respectively. The ITO film shows a homogeneous surface with small grains around 30-40 nm wide. The low contrast of the grain boundaries suggests that they have no sharp edges, which could indicate the presence of an important fraction of the amorphous phase, as anticipated by the XRD data for the films grown at high temperature. On the contrary, the AZO film surface is inhomogeneous, made of islands around 100 nm wide with straight sides. As shown in the inset of Fig. 3b (120×120 nm^2), each of these islands is, in turn, made of aggregated small crystallites 10-20 nm wide. While limited by the system resolution, these crystallites are most likely highly oriented hexagonal structures closed packed in larger islands, as suggested the XRD data and the high contrast of the crystallites edges. These islands are arranged in a horizontal layered structure, in agreement with the reduced vertical grain size of ~30 nm calculated from the XRD peak width.

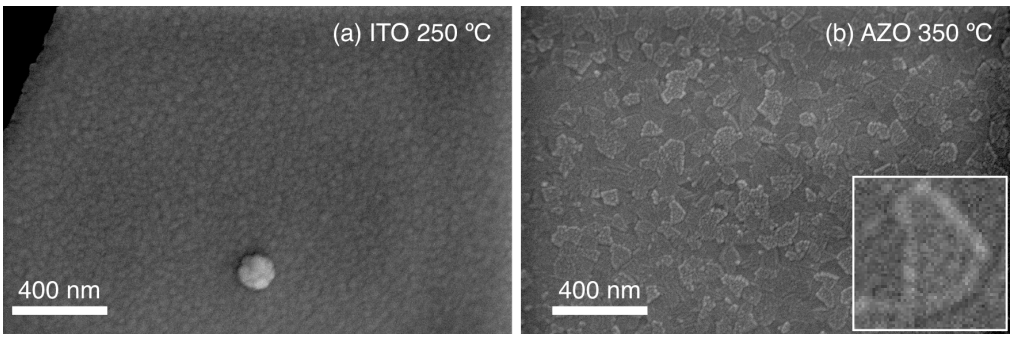

Fig. 3. SEM images of the (a) ITO film grown at 250 ºC and (b) of the AZO film grown at 350 ºC. The inset in (b) shows a detail of one of the AZO islands (120×120 nm^2).

3.2 Optical Properties: Ellipsometry

The ellipsometry data is fitted with a Tauc-Lorentz-Drude model. The Tauc-Lorentz oscillator accounts for the band-to-band absorption and the properties in the UV-visible region of the spectrum whilst the Drude oscillator accounts for the free carrier absorption in the infrared. In all cases, surface roughness is included in the calculation as described in Woollam et al. [36]. The use of models rather than a point-by-point fitting of the ellipsometry data to n and k is necessary in order to obtain physically sound results in the regions where $k << n$ and the ellipsometry signal is dominated by n.

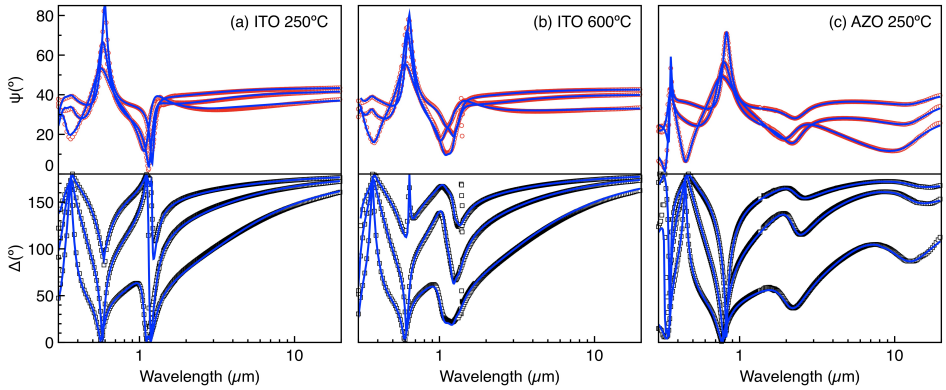

Fig. 4. Examples of the ellipsometry measurements (symbols) and fitting (blue line). (a) The ITO film grown at 250ºC, (b) the ITO film annealed at 600ºC, and (c) the AZO film grown at 250ºC.

For the ITO films grown at high temperatures a single homogeneous layer (plus roughness) is sufficient to produce a good fit between the experimental data and the model. Fig. 4a shows an example of such a fitting of the ellipsometry data for the film grown at 250 ºC. The calculated optical constants, presented in Fig. 5a, are very similar in the three cases, consistent with the small changes in crystallinity and crystal orientation observed in the XRD measurements. Contrary to the films grown at high temperature, the films grown at room temperature and then annealed required a graded layer to obtain a good fit, illustrated in Fig. 4b. Such dependence of the film properties with the depth are often observed in ITO films [19,36] and associated with a gradient in the doping, the granularity and/or the porosity of the film. Fig. 5b shows the n and k data of the RT film and the films annealed at 500 ºC and 600 ºC. The optical bandgap of the ITO varies considerably between samples. All the films grown at high temperature have the absorption edge at around 325 nm (3.81 eV), which is within the range of the reported data [24,34]. The film grown at room temperature and those annealed show the absorption edge at nearly 400 nm (3.1 eV) and a significant variation between the top and the bottom of the film. This difference is generally attributed to a change in the carrier concentration [24], although the density of the film might also play a role specially in the abruptness of the transition.

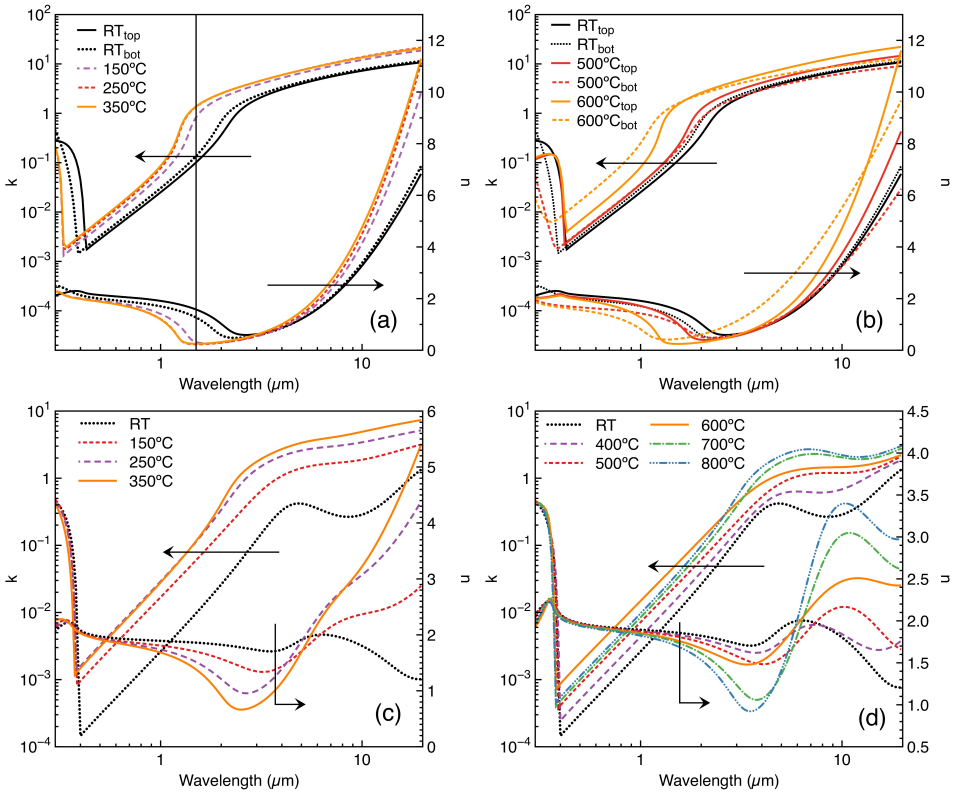

Fig. 5. The refractive index (n) and extinction coefficient (k) of (a) ITO films grown at high temperature, (b) selected, annealed ITO films, (c) AZO films grown at high temperature and (d) annealed AZO films.

The AZO films present a similar qualitative behaviour to the ITO films; a good fit is achieved using a homogeneous layer, but requires an extra Lorentz-type oscillator in the MIR, in addition to the Drude component (Fig. 4c). Besides this unexpected component, which will be discussed in detail in Section 4, the optical-constant curves in Fig. 5c and 5d show that the absorption edge is almost independent of the deposition conditions or annealing process, being always in the 350-365 nm range (3.4-3.5 eV). They also demonstrate that the extinction coefficients are higher for the samples processed at higher temperatures, either grown or annealed, which is associated with an increase in the free carrier density and mobility, compared to the samples processed at low temperature.

A key parameter that identifies conductive materials is the wavelength of the zero-crossover of the real part of the permittivity, which is related to the plasma frequency in the Drude free-electron model. For noble metals like gold or silver, the transition occurs in the ultraviolet. For both ITO and AZO films, it is found in the near-IR (1.3-1.5 μm) [37,38]. In our case, the ITO films grown at high temperature and the films annealed at temperatures of 600 ºC or higher show a crossover also in the near-IR (1.1-1.4 μm), but the room temperature film and those annealed at 400 ºC and 500 ºC have a crossover at a much longer wavelength, from 1.8 to 2.2 μm (Fig. 6a). Furthermore, of all the AZO films, only those grown at 250 ºC and 350 ºC demonstrate a single zero-crossover in the NIR: at 2.25 and 2.62 μm respectively (Fig. 6b). Films annealed at 700 ºC and 800 ºC show an oscillatory behaviour with two crossovers between 3.4 to 7.0 μm, and the rest of the films only show a crossover beyond 12 μm. Overall, the trend exhibited by these latter films is more compatible with a highly doped semiconductor below the metal-insulator transition.

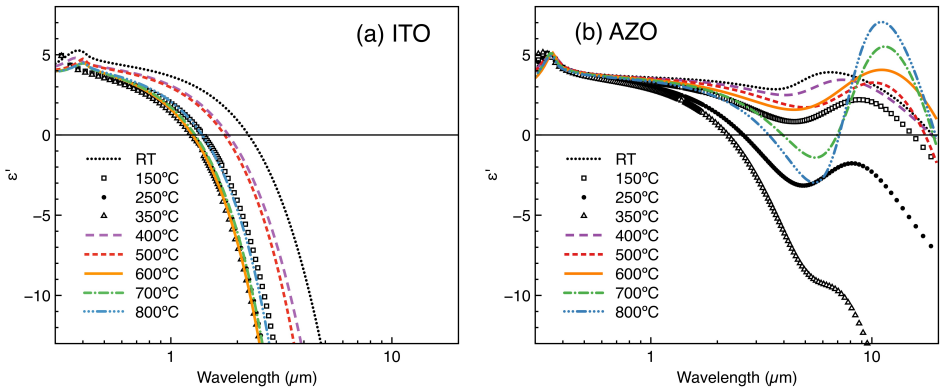

Fig. 6. Real part of the complex dielectric constant for all (a) ITO and (b) AZO films. For the ITO, only the dielectric constant corresponding to the top of the layers is shown.

3.3 Electrical Properties: Hall & Resistivity

The mobility and resistivity of the films were measured using the 4-point probe (4p) technique and Hall measurements. Additionally, the resistivity was derived from the Drude component of the models used to fit the ellipsometry data for each sample. The results are presented in Fig. 7. For the annealed ITO samples, which are inhomogeneous and require a graded optical model to fit the ellipsometry data, the calculated resistivities at the top and bottom of the film are included.

The resistivity of all ITO films is found to be between 0.1 and 1 mΩ-cm (Fig. 7a), with good general agreement between the three methods. Films grown at high temperature have the lowest resistivity from ~0.5 mΩ-cm for the film grown at 150 ºC to 0.2 mΩ-cm for that at 350 ºC. Films annealed at 800 ºC show a resistivity as low as 0.1 mΩ-cm near the top surface according to the ellipsometry results, but the average resistivity of the film as measured by 4p or Hall is around 0.3 mΩ-cm, as the bottom of the layers is much more resistive. Overall higher temperature processing yields the lowest resistivity, with values of 0.1-0.2 mΩ-cm obtained and in in the range of the state of the art for ITO films [1]. Both carrier densities and mobilities are also in the typical range for this material, 5-15x10^{20} cm^{-3} and >20 cm^2 $V^{-1}s^{-1}$, respectively. The mobility and the average scattering time of the layer are related by the carrier effective mass m* through $\mu = q\tau/m^*$. Plotting the mobility against the scattering time and fitting to a straight line (not shown) results in an effective mass of $m^* = (0.39 \pm 0.07)\ m_0$, with m_0 the electron rest mass. The 150 ºC sample was excluded from the fitting as an outlier.

For the AZO films grown at high temperature, the agreement between the resistivities obtained by the different techniques is very good, producing values in the 10 to 1 mΩ-cm for the 150 ºC to 350 ºC samples, respectively, carrier densities over 10^{20} cm^{-3}, and Hall mobilities between 6 and 30 cm^2 V^{-1} s^{-1}. These resistivities are at the higher end of the values often found in the literature [21,26,39]. Conversely, the resistivities obtained for annealed AZO films show significant discrepancies between the electrical and the optical measurements derived from the Drude model. The resistivities resulting from the latter are again in the <10 mΩ-cm range, decreasing with temperature down to 3 mΩ-cm for the 800 ºC film. This is in good agreement with the trends observed from the XRD peak shift associated with the activation of dopants. Electrical measurements, however, demonstrate much higher values, up to 100 times higher in the case of the film annealed at 700 ºC. Moreover, a non-obvious trend can be deduced from the dependence of the resistivity with the annealing temperature. We associate this discrepancy to a strong electrical in-plane inhomogeneity of the films when the density of active dopants is low, as pointed out when describing the ellipsometry results in Section 3.2. Similarly, no linear relation is found between the mobility and the scattering time, meaning an effective mass cannot be calculated.

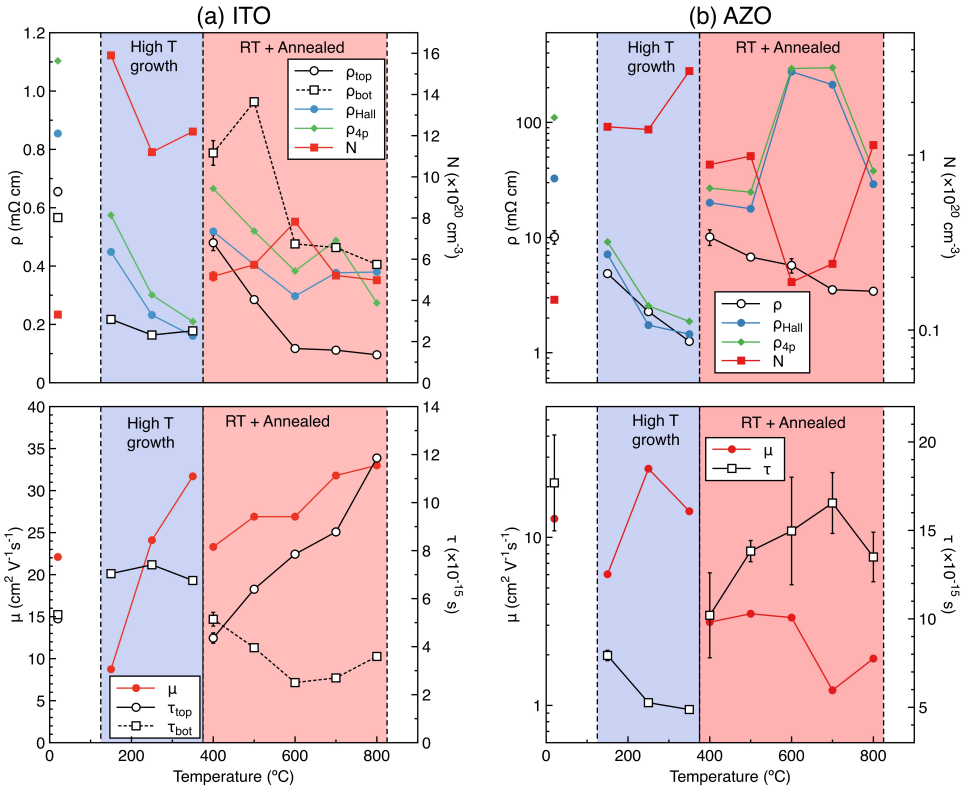

Fig. 7. Resistivity ρ, carrier density N, scattering time τ and mobility μ of all the (a) ITO and (b) AZO films. Open symbols for ρ and τ are the adjustable parameters of the Drude model in the ellipsometry fits.

4. Discussion

4.1 AZO with low dopant density

The low temperature annealed AZO films show behavior that more closely resembles a disordered heavily-doped semiconductor than a metal. Das et al. [39] showed that below an aluminium concentration of 0.2%, there is a very strong dependence of the carrier density and resistivity of the AZO films with the dopant density. In this regime, small fluctuations in the active dopants results in a metal-insulator transition, changing abruptly the electrical and optical properties of the material. Spatial fluctuations of that order are often observed in the growth of AZO films by sputtering [40]. In the lower-doped semiconducting regions, carriers will be quasi-bound, and therefore do not demonstrate the Drude-like free-carrier behaviour, but rather a resonance with non-zero central energy in the MIR region. As the carrier density increases – either because of an increase of the dopant density or through the activation of the existing dopants with annealing – the MIR resonance shifts to lower energies and eventually obeys the Drude-like free carrier absorption model. Fig. 8 shows the central energy (wavelength) of the Lorentz oscillator used to fit the AZO ellipsometry data, where this shift is clearly observed. Such a trend in the optical properties during the semiconductor-to-metal transition depends on the specific crystal structure and localization of the electronic orbitals. It has been described for transition metal oxides in the context of high temperature superconductors, but has not been

reported for AZO alloys [41]. The underlying mechanism leading to this transition it is yet to be determined for this material.

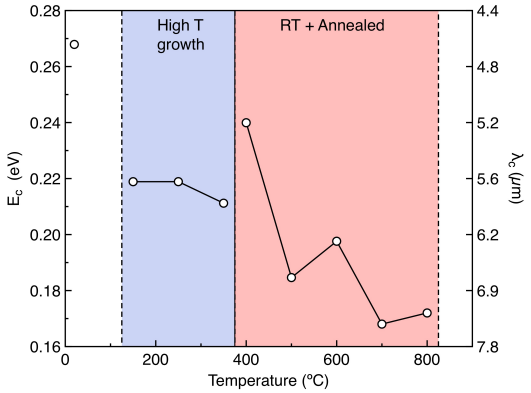

Fig. 8. Central energy of the Lorentz oscillator used to fit the ellipsometry of the AZO films.

The discrepancy between the optical and electrical data can now be understood in terms of the inhomogeneity of the films. Ellipsometry is performed over a relatively large area, ranging from 71 to 160 mm^2 depending on the angle, and it can discriminate between the different optical behaviour of distinct regions of the sample: the Drude component used during the fitting of the ellipsometry data is related to the metallic regions and the Lorentz component represent the regions with lower doping that have not undergone the metal-insulator transition to become metallic. For the electrical measurements, the samples are smaller (25 mm^2) and they can only provide average values for the properties of the films: depending on the dominant character of the AZO layer of that particular area, the resulting electrical properties will be those of a more or less conductive sample, resulting in the erratic trend shown in Fig. 7b. In this case, the electrically determined resistivity will appear higher, as it averages conductive and non-conductive regions, as opposed to the Drude values that only represent the conductive regions.

4.2 Films as low emissivity coatings

To assess the performance of the above films as low emissivity coatings we have used a transfer matrix algorithm to calculate how the radiation couples in and out of the solar cell – solar radiation in the visible and near-IR, and thermal radiation in the MIR. We use a stack made of the TCO film (variable thickness and material), highly doped silicon (450 μm, measured *n* and *k*) and a back surface of aluminium (200 nm, tabulated values). It is important that the suitability of the film is assessed together with the rest of the layers, and not as a standalone material, given that the absorptivity (=emissivity) will depend on the optical properties of the structure as a whole. Compared with a real silicon solar cell, this three-layer planar structure has some simplifications, such as the lack of surface texture or thicker substrate. We will discuss in section 4.4 the effect that those simplifications have on the results.

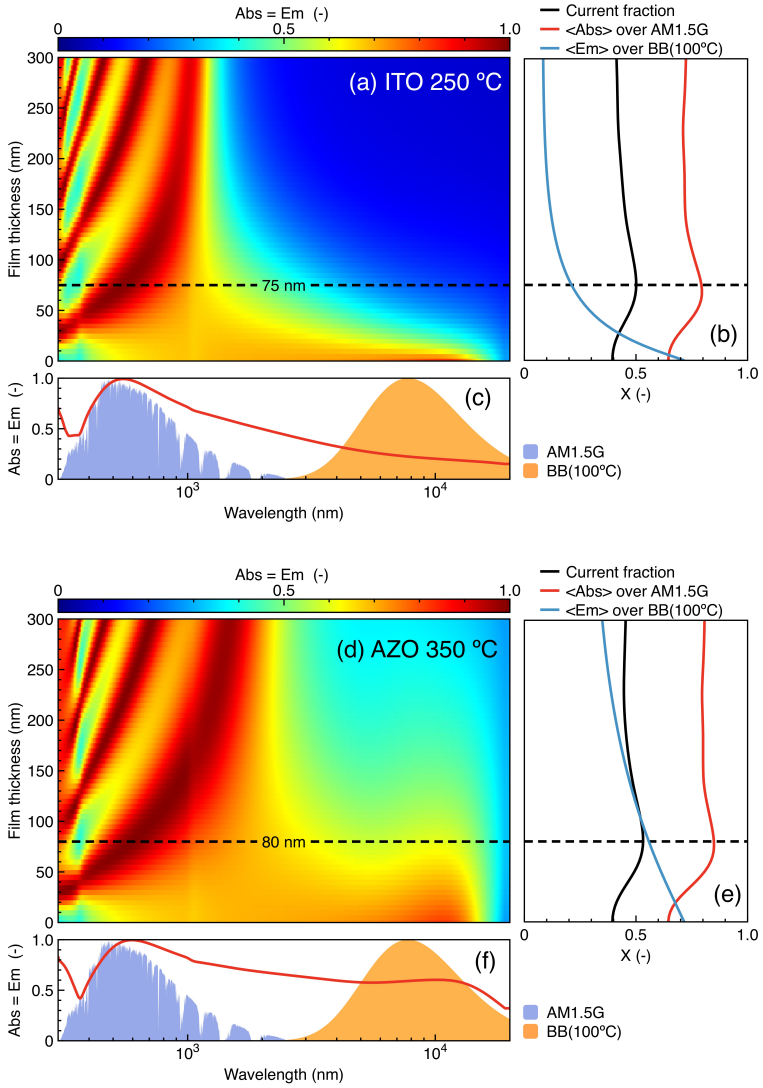

Fig. 9. The calculated absorptivity using the ITO 250 ºC and AZO 350 ºC films properties. (a) and (d) are absorptivity maps vs wavelength and film thickness. (b) and (e) are fraction of absorbed current <Abs> over AM1.5G and <Em> over BB (100ºC). (c) and (f) are absorptivity at the thickness that yields the maximum fraction of absorbed current, together with the normalized AM1.5G and BB (100ºC) spectra.

Fig. 9 demonstrates the absorptivity results for TCO layers of different thicknesses calculated using the properties of the ITO 250 ºC and AZO 350 ºC films. These two materials and conditions are chosen as they form homogeneous layers and exhibit the best electrical properties of all the films studied in this paper. Two distinct regions can be observed as a function of the wavelength, associated with the regions where the TCOs are transparent and absorptive. At short wavelengths (visible and near-IR) the films are transparent and light couples into the silicon substrate. Depending on the thickness of the layers, one or more interference fringes can be observed, associated with regions of maximum and minimum reflection of the radiation. This is the usual observation from anti-reflecting coatings. At longer wavelengths (>1200 nm or >2500 nm for ITO and AZO respectively) the films become both absorptive and highly reflective. In this range, increasing the film thickness reduces the

absorptivity as the underlying silicon substrate is decoupled from the outside medium (air). Such a limiting situation is reached for the ITO film in a few hundred nanometres but requires around a μm for the AZO as a result of the lower extinction coefficient *k*.

To evaluate the performance of these films as low emissivity coatings in PVT applications, three parameters must be calculated: the fraction of the photon current absorbed in the silicon substrate above the bandgap, $f_{current}$, (which leads to the electrical current), the fraction of solar power absorbed in the whole sample, <Abs>, (average absorptivity in the visible and near-IR) and the fraction of thermal radiation emitted by the sample, <Em>, (average emissivity in the mid-IR). These parameters are calculated as:

$$f_{current} = \frac{\int_0^{\lambda_g(Si)} Abs_{Si}(\lambda) \times AM1.5g(\lambda) \frac{\lambda}{1240} d\lambda}{\int_0^{\infty} AM1.5g(\lambda) \frac{q\lambda}{hc} d\lambda}) \quad [1]$$

$$< Abs >= \frac{\int_0^{\infty} Abs(\lambda) \times AM1.5g(\lambda) d\lambda}{\int_0^{\infty} AM1.5g(\lambda) d\lambda} \quad [2]$$

$$< Em >= \frac{\int_0^{\infty} Em(\lambda) \times BB(100ºC)(\lambda) d\lambda}{\int_0^{\infty} BB(100ºC)(\lambda) d\lambda} \quad [3]$$

with *q* the electron charge, *h* the Plank's constant, *c* the speed of light, *Abs* the total absorptivity of the structure and Abs_{Si} the absorptivity of only the silicon layer, excluding the TCO and the aluminium back contact. An ideal hybrid PVT system will have $f_{current}$ and <Abs> as close to unity as possible while <Em> approaches zero. For the calculation of these parameters we use the air mass 1.5 global solar spectrum, AM1.5G [42], and the spectrum of a black body at 100 ºC, BB(100ºC), as an illustrative temperature for emissivity control in a PVT collector. Fig. 9b and 9e show the calculated values as a function of the film thickness for the ITO and AZO films. In both cases, the current fraction and the average absorptivity show a maximum for thicknesses around 70-80 nm. For this thickness, the AR function of the TCO coating allows the maximum amount of sunlight to enter the silicon substrate. Thicker values of the films result in lower fractional current and average absorptivity because of an increased average reflection. The average emissivity, on the contrary, decreases with increasing film thickness. Table 1 lists the different parameters at the maximum of the current fraction, taken as the optimum condition to maximize electrical output, and Fig. 9c and 9f demonstrate the corresponding absorptivity.

Based on these results, a 75 nm thick ITO film will be superior to a 80 nm thick AZO film as low emissivity coating: the ITO layer shows a slightly lower current fraction and average absorptivity, but the much lower emissivity ensures a higher working temperature or output power flux at a given temperature, as we discuss in the next section.

Table 1. Current fraction, average absorptivity and emissivity at the film thickness maximizing the current fraction

	Thickness (nm)	$f_{current}$	<Abs>	<Em>
ITO	75	0.5	0.79	0.21
AZO	80	0.53	0.85	0.58

4.3 Thermodynamical power balance model

To further illustrate the potential performance of these films as low emissivity coatings for PVT systems, the maximum extracted power as a function of the operating temperature of the system has been calculated using a simple thermodynamical power balance analysis. In equilibrium, the overall power flux going into the solar cell and coming out of it must balance. In a solar

collector facing the Sun with only radiative coupling with its surroundings, there are four fluxes to consider: the power coming from the Sun, P_{Sun}, and the thermal radiation from the ambient, P_A, absorbed by the solar cell, on one hand, and the thermal radiation emitted by the collector to the ambient, P_{Cell}, and the extracted power, P_E, – which includes thermal and electrical power – on the other.

$$P_{Sun} + P_A(T_A) = P_{cell}(T_{cell}) + P_E \quad [4]$$

where T_A and T_{cell} are the temperatures of the ambient and the cell. The maximum power that can be extracted from a solar cell – in any form – can therefore be calculated as a function of the cell temperature, the ambient temperature and the solar irradiance. This will represent an absolute upper limit of any practical design for a hybrid PVT collector. The power absorbed/emitted by the solar cell can be calculated in terms of the emissivity *Em(λ)* as:

$$P(\mathrm{T}) = \int \mathrm{Em}(\lambda)\mathrm{S}(\lambda, \mathrm{T})\mathrm{d}\lambda \quad [5]$$

with S(λ,T) the spectral irradiance of the incoming/outgoing radiation. For sunlight, the spectral irradiance will be given by the *AM1.5g* at 1 sun of concentration, as above. For the thermal radiation of the ambient (incoming) and the solar cell (outgoing) we use Plank's law for black body radiation *BB(λ, T)* at T_A = 25 ºC and T_{cell}, respectively, integrated over a hemisphere to consider that radiation is absorbed/emitted in all directions at the front surface. Combining Eq. 4 and 5 and re-arranging terms, we get:

$$P_E(T) = \int Em(\lambda)\big(AM1.5G(\lambda) + \pi BB(\lambda, T_A) - \pi BB(\lambda, T_{cell})\big)d\lambda \quad [6]$$

Fig. 10a shows the emissivity of the ITO and AZO films on top of a silicon substrate that were concluded as optimal in the previous section (the same curves as in Fig. 9c and 9f above). Two more curves are included: the target emissivity for a nearly ideal PVT collector, with absorptivity equal to one in the range of the solar spectrum and very low emissivity in the MIR range; and the emissivity of a typical diffused back surface field silicon solar cell. Details of the origin of the emissivity of this type of solar cell are discussed by Riverola et al. [43].

The calculated extracted power using Eq. 6 for each of these four emissivities (Fig. 10b) demonstrates a few key results to understand the role of spectrally selective coatings. First, at low cell temperatures (<60 ºC), the extracted power is dominated by the amount of solar radiation absorbed by the structure. The silicon solar cell, as a consequence, shows better performance, followed by the AZO film and the ITO film, which were shown to have <Abs> equal to 0.85 and 0.79, respectively (Table 1). As it will be discussed in the next section, this higher absorptivity of the silicon cell is the result of the surface texture, which is not present in the ITO or AZO structures.

At higher temperatures, the much lower emissivity of the TCO films compared to the silicon cell dominates the extracted power. In particular, at 100 ºC, the AZO coated structure could deliver 20% more power than the silicon cell and over 50% in the case of the ITO coated structure. Considering the target emissivity – which is typical of purely thermal systems – as a sensible upper limit, another 50% enhancement should be achievable with a fully optimized surface, including both low emissivity coating and textures.

Conversely, for a given extracted power, the ITO film allows for a higher operating temperature than the AZO film or the silicon solar cell. For example, if 500 Wm^{-2} are extracted, the silicon cell will operate at 90 ºC, the AZO coated structure at 100 ºC and the ITO at around 150 ºC. While these high temperature heat widens the application range of the system from the thermal point of view, it should be noted that photovoltaic solar cells perform fundamentally worse at those temperatures and therefore the electrical power output will drop [9].

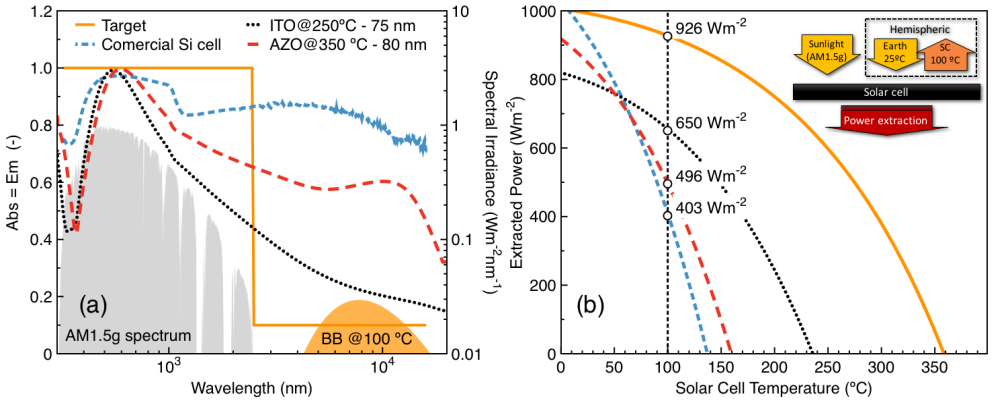

Fig. 10. (a) The calculated absorptivity using the ITO 250 ºC and AZO 350 ºC films, together with the absorptivity of a commercial silicon solar cell and a target, nearly ideal, absorptivity. (b) Calculated extracted power as a function of the cell temperature. The inset shows a schema of the thermodynamical power balance calculation.

4.4 Limitations of the analysis

The modelling described above is simple and presents a good qualitative description of the performance of the TCO films as low emissivity coatings, as well as the role that their properties play. However, there are two important limitations.

The first limitation concerns the materials used. As discussed, the ITO films described in this paper – in particular those grown at high temperature - are close to the state of art ITO films reported in the literature but the AZO films are not. Despite the AZO films having sensible resistivity and mobility values, adequate for many applications, more homogeneous films that are fully metallic, above the metal-insulator transition, could have a similar or better performance than the ITO coatings. Therefore, further optimization of our growth process and post-processing for AZO films is desirable.

The second limitation concerns the fact that terrestrial silicon solar cells employ surface texturing to reduce the reflection and enhance the absorption of long wavelength photons by increasing the optical path length inside the cell. We tackle the second issue simply by using a relatively thick substrate compared to the usual thicknesses found in industry (150-250 μm). Nevertheless, not having a textured surface in our model still imposes an important limitation for the quantitative analysis reported in this work. For a textured silicon solar cell, we expect current fractions in the order of 0.58-0.59 (equal to a current density of 40-41 mA/cm^2), rather than 0.5-0.53 (equal to 34.5-36.6 mA/cm^2), the maximum for crystalline silicon being 0.625 (equal to 43.2 mA/cm^2).

A texture will increase the absorptivity at all wavelengths, including in the MIR, and therefore an increase in the minimum emissivity attainable in textured devices is expected. The interplay between the thin TCO layers (~100 nm) and the relatively large textured features (~μm) is not straightforward either. Simulating such a situation requires more sophisticated modelling than the simple planar transfer matrix approach used in this paper. In that case, the typical size of the textured features will be comparable to the wavelength of the radiation, which could require a full electromagnetic theory treatment in the model. A multi-scale approach like the one described by Riveola et al. will be used in the future for the optimization of low emissivity coatings in textured surfaces [43].

5. Conclusions

In this work, we have presented a thorough analysis of the electrical and optical properties over a broad spectral range (300 nm to 20 μm) of ITO and AZO films fabricated and annealed at different temperatures. The specific application of the films was their combined use as front transparent electrode and low thermal emissivity coating for silicon-based solar cells indented for hybrid solar photovoltaic-thermal collectors.

Our results demonstrate that a single ITO layer, around 75 nm thick, deposited directly on the silicon substrate at 250 ºC allows for the best trade-off between sunlight transmittance into the solar cell (0.79 average absorptivity over the solar spectrum), thermal emission suppression (0.21 average emissivity over the blackbody spectrum at 100 ºC) and electrical transport, with a resistivity near the state-of-the-art for this material (0.1-0.2 mΩ-cm). AZO films, whilst showing superior transparency and sunlight coupling into the solar cell than ITO films (0.85 average absorptivity), also demonstrated poorer electrical transport properties and thermal emission suppression. This result is not a fundamental limitation of the material, however, but rather a consequence of the specific deposition conditions used in this work, resulting in the AZO films being very close or even below the metal-insulator transition.

In that regard, this is the first time that the metal-insulator transition has been characterized for AZO from the optical point of view. Our preliminary results demonstrate that before undergoing such transition, the optical properties of the material in the MIR are characterised by a Lorentz type oscillator that we tentatively associate to the interaction of light with quasi-bound electrons. Further work is in progress to fully determine the underlying mechanism leading to this transition.

A final point to mention is the possibility of using multi-layer coatings to achieve even lower emissivity and keep good transparency in the visible. That is a common approach, and indeed the coating used by Lämmle et al. that reaches the best reported performance uses up to 6 layers including two AZO layers and one silver layer [8]. By using a single layer, in this work we have favoured the simplicity of fabrication and cost reduction of the ultimate final product. More importantly, it makes the low emissivity coating compatible with the role of the front electrode in solar cells – in particular of SHJ cells – something that is not possible in the previously reported multi-layered coatings.

References

1. Ellmer, Klaus (2012) Past achievements and future challenges in the development of optically transparent electrodes. *Nature Photonics*, **6**, 1–9.
2. Green, Martin A (2007) Thin-film solar cells: review of materials, technologies and commercial status. *J Mater Sci: Mater Electron*, **18**, 15–19.
3. Khalil, Asma, Ahmed, Zubair, Touati, Farid, Masmoudi, Mohamed (2016) Review on organic solar cells. *Proceedings of the 13th International Multi-Conference on Systems, Signals and Devices*, 342–353.
4. Louwen, Atse, van Sark, Wilfried, Schropp, Ruud, Faaij, André (2016) A cost roadmap for silicon heterojunction solar cells. *Solar Energy Materials and Solar Cells*, **147**, 295–314.
5. Jelle, Bjørn Petter, Kalnæs, Simen Edsjø, Gao, Tao (2015) Low-emissivity materials for building applications: A state-of-the-art review and future research perspectives. *Energy & Buildings*, **96**, 329–356.
6. Runnerstrom, Evan L, S, Anna Llord, Lounis, Sebastien D, Milliron, Delia J (2014) Nanostructured electrochromic smart windows: traditional materials and NIR-selective plasmonic nanocrystals. *Chem. Commun.*, **50**, 10555–10572.
7. Ehrmann, N, Reineke-Koch, R, Föste, S, Giovannetti, F (2013) The influence of

process parameters and coating properties of double glazing coated with transparent conducting oxides on the efficiency of solar-thermal flat-plate collectors. *Thin Solid Films*, **532**, 132–140.
8. Lämmle, M, Kroyer, T, Fortuin, S, et al. (2016) Development and modelling of highly-efficient PVT collectors with low-emissivity coatings. *Solar Energy*, **130**, 161–173.
9. Mellor, Alexander, Alonso-Álvarez, Diego, Guarracino, Ilaria, et al. Emissivity control in hybrid photovoltaic thermal generators for improved exergy efficiency. In preparation for *Energy and Environmental Science* (2017).
10. Jiang, L, Lan, C, Kim, Y S, Ma, Y (2013) An evacuated PV/Thermal hybrid collector with the tube/XCPC design. *Proceedings of World Renewable Energy Forum 2013*, 88–94.
11. Naked Energy. nakedenergy.co.uk.
12. Guarracino, Ilaria, Mellor, Alexander, Ekins-Daukes, Nicholas J, Markides, Christos N (2016) Dynamic coupled thermal-and-electrical modelling of sheet-and-tube hybrid photovoltaic/thermal (PVT) collectors. *Applied Thermal Engineering*, **101**, 778–795.
13. van Sark, Wilfried, Korte, Lars, Roca, Francesco (2012) Physics and Technology of Amorphous-Crystalline Heterostructure Silicon Solar Cells, Springer Berlin Heidelberg, Berlin, Heidelberg.
14. Bedia, F Z, Bedia, A, Aillerie, M, et al. (2014) Influence of Al-doped ZnO Transparent Contacts Deposited by a Spray Pyrolysis Technique on Performance of HIT Solar Cells. *Energy Procedia*, **50**, 853–861.
15. Khranovskyy, V, Grossner, U, Lazorenko, V, et al. (2007) Conductivity increase of ZnO:Ga films by rapid thermal annealing. *Superlattices and Microstructures*, **42** (1-6), 379–386.
16. Jun, Min-Chul, Park, Sang-Uk, Koh, Jung-Hyuk (2012) Comparative studies of Al-doped ZnO and Ga-doped ZnO transparent conducting oxide thin films. *Nanoscale Res Lett*, **7**, 639.
17. Boudiar, T, Sandu, C S, Canut, B, Blanchin, M G (2003) Interest of rapid thermal annealing (RTA) for the elaboration of SnO2: Sb transparent conducting oxide by the sol-gel technique. *Journal of Sol-Gel Science and Technology*, **26**, 1067-1070.
18. Craciun, V, Craciun, D, Wang, X, et al. (2003) Transparent and conducting indium tin oxide thin films grown by pulsed laser deposition at low temperatures. *Journal of Optoelectronics and Advanced Materials*, **5**, 401–408.
19. Solieman, A, Aegerter, M A (2006) Modeling of optical and electrical properties of In2O3:Sn coatings made by various techniques. *Thin Solid Films*, **502**, 205–211.
20. Dhakal, Tara, Nandur, Abhishek S, Christian, Rachel, et al. (2012) Transmittance from visible to mid infra-red in AZO films grown by atomic layer deposition system. *Solar Energy*, **86**, 1306–1312.
21. Yang, Weifeng, Liu, Zhuguang, Peng, Dong-Liang, et al. (2009) Room-temperature deposition of transparent conducting Al-doped ZnO films by RF magnetron sputtering method. *Applied Surface Science*, **255**, 5669–5673.
22. Seo, Seung-Woo, Won, Sung Ho, Chae, Heeyeop, Cho, Sung Min (2012) Low-temperature growth of highly conductive and transparent aluminum-doped ZnO film by ultrasonic-mist deposition. *Korean Journal of Chemical Engineering*, **29**, 525–528.
23. Shih, Neng-Fu, Chen, Jin-Zhou, Jiang, Yeu-Long (2013) Properties and Analysis of Transparency Conducting AZO Films by Using DC Power and RF Power Simultaneous Magnetron Sputtering. *Advances in Materials Science and Engineering*, **2013**, 1–6.
24. Song, Shumei, Yang, Tianlin, Liu, Jingjing, et al. (2011) Rapid thermal annealing of ITO films. *Applied Surface Science*, **257**, 7061–7064.
25. Gulen, M, Yildirim, G, Bal, S, et al. (2012) Role of annealing temperature on microstructural and electro-optical properties of ITO films produced by sputtering. *J Mater Sci: Mater Electron*, **24**, 467–474.

26. Ben Ayadi, Z, Mir, El, L, Djessas, K, Alaya, S (2009) Effect of the annealing temperature on transparency and conductivity of ZnO:Al thin films. *Thin Solid Films*, **517**, 6305–6309.
27. Geng, Y, Xie, Z Y, Xu, S S, et al. (2012) Effects of Rapid Thermal Annealing on Structural, Luminescent, and Electrical Properties of Al-Doped ZnO Films Grown by Atomic Layer Deposition. *ECS Journal of Solid State Science and Technology*, **1**, N45–N48.
28. Choi, S Y, Choi, K, Kim, S J (2013) Rapid thermal annealing effects on the electrical and structural properties of the AZO thin film deposited at a room temperature, *Int. J. Adv. Res. Electr. Electron. Instrum. Eng.* **2**, 6034-6043
29. Li, C, Furuta, M, Matsuda, T, et al. (2009) Effects of substrate on the structural, electrical and optical properties of Al-doped ZnO films prepared by radio frequency magnetron sputtering. *Thin Solid Films*, **517**, 3265–3268.
30. Shen, Hong-lie, Zhang, Hui, Lu, Lin-feng, et al. (2010) Preparation and properties of AZO thin films on different substrates. *Progress in Natural Science: Materials International*, **20**, 44–48.
31. hamali, El, S O, Cranton, W M, Kalfagiannis, N, et al. (2016) Enhanced electrical and optical properties of room temperature deposited Aluminium doped Zinc Oxide (AZO) thin films by excimer laser annealing. *Optics and Lasers in Engineering*, **80**, 45–51.
32. Sorar, I, Saygin-Hinczewski, D, Hinczewski, M, Tepehan, F Z (2011) Optical and structural properties of Si-doped ZnO thin films. *Applied Surface Science,* **257**, 7343–7349.
33. Xu, Jiwen, Yang, Zupei, Zhang, Xiaowen, et al. (2013) Grain size control in ITO targets and its effect on electrical and optical properties of deposited ITO films. *J Mater Sci: Mater Electron*, **25**, 710–716.
34. Meng, L H, Placido, F (2003) Annealing effect on ITO thin films prepared by microwave-enhanced dc reactive magnetron sputtering for telecommunication applications. *Surface & Coatings Technology*, **166**, 44–50.
35. Lin, Y M, Chu, C H, Wu, H W, Huang, L (2015) Study of AZO Thin Films Under Different Annealing Atmosphere on Structural, Optical and Electrical Properties by rf Magnetron Sputtering. *Proceedings of the International MultiConference of Engineers and Computer Scientists*, **2**, 807–810.
36. Woollam, J A, McGahan, W A, Johs, B (1994) Spectroscopic Ellipsometry Studies of Indium Tin Oxide and Other Flat-Panel Display Multilayer Materials. *Thin Solid Films*, **241**, 44–46.
37. Kim, J, Naik, G V, Emani, N K, Guler, U (2013) Plasmonic resonances in nanostructured transparent conducting oxide films. *IEEE J. Select. Topics Quantum Electron.*, **19**, 4601907–4601907.
38. Rajak, Sukla, Ray, Mina (2014) Comparative study of plasmonic resonance in transparent conducting oxides: ITO and AZO. *Journal of Optics*, **43**, 231–238.
39. Das, Amit K, Misra, P, Ajimsha, R S, et al. (2012) Studies on temperature dependent semiconductor to metal transitions in ZnO thin films sparsely doped with Al. *J. Appl. Phys.*, **112**, 103706–7.
40. Crovetto, Andrea, Ottsen, Tobias Sand, Stamate, Eugen, et al. (2016) On performance limitations and property correlations of Al-doped ZnO deposited by radio-frequency sputtering. *Journal of Physics D: Applied Physics*, **49**, 1–11.
41. Uchida, S, Eisaki, H, Tajima, S (1993) Electron correlation and optical conductivity in high-Tc copper oxides—origin of the mid-infrared absorption band. *Physica B: Condensed Matter*, **186-188**, 975–980.
42. ASTM International, G03 Standard Tables for Reference Solar Spectral Irradiances: Direct Normal and Hemispherical on 37° Tilted Surface. www.astm.orgcgi-binresolver.cgiG.

43. Riverola-Lacasta, Alberto, Mellor, Alexander, Alonso-Álvarez, Diego, et al. Mid-infrared emissivity of crystalline silicon solar cells. *Submitted to Progress in Photovoltaics* (2017).

Acknowledgement

This work was funded by the Engineering and Physical Science Research council (EPSRC) grant EP/M025012/1. A. Mellor was supported by the European Commission through Marie Sklodowska Curie International Fellowship, Grant No. DLV-657359.